C/NOFS measurements of magnetic perturbations in the low-latitude ionosphere during magnetic storms

Guan Le,[1] William J. Burke,[2,3] Robert F. Pfaff,[1] Henry Freudenreich,[1] Stefan Maus,[4] and Hermann Lühr[5]

Received 26 July 2011; revised 24 October 2011; accepted 25 October 2011; published 28 December 2011.

[1] The Vector Electric Field Investigation suite on the C/NOFS satellite includes a fluxgate magnetometer to monitor the Earth's magnetic fields in the low-latitude ionosphere. Measurements yield full magnetic vectors every second over the range of ±45,000 nT with a one-bit resolution of 1.37 nT (16 bit A/D) in each component. The sensor's primary responsibility is to support calculations of both $\mathbf{V} \times \mathbf{B}$ and $\mathbf{E} \times \mathbf{B}$ with greater accuracy than can be obtained using standard magnetic field models. The data also contain information about large-scale current systems that, when analyzed in conjunction with electric field measurements, promise to significantly expand understanding of equatorial electrodynamics. We first compare in situ measurements with the POMME (Potsdam Magnetic Model of the Earth) model to establish in-flight sensor "calibrations" and to compute magnetic residuals. At low latitudes the residuals are predominately products of the storm time ring current. Since C/NOFS provides a complete coverage of all local times every 97 min, magnetic field data allow studies of the temporal evolution and local time variations of storm time ring current. The analysis demonstrates the feasibility of using instrumented spacecraft in low-inclination orbits to extract a timely proxy for the provisional Dst index and to specify the ring current's evolution.

Citation: Le, G., W. J. Burke, R. F. Pfaff, H. Freudenreich, S. Maus, and H. Lühr (2011), C/NOFS measurements of magnetic perturbations in the low-latitude ionosphere during magnetic storms, *J. Geophys. Res.*, *116*, A12230, doi:10.1029/2011JA017026.

1. Introduction

[2] The morphology and evolution of the ring current are critical issues for understanding inner magnetospheric dynamics during magnetic storms. Westward flowing currents produce southward magnetic perturbations near the equator on Earth that are antiparallel to the main field. As the storm time ring current intensifies the horizontal component of the geomagnetic field becomes increasingly depressed at low latitudes on the ground. These magnetic perturbations provide a convenient tool to monitor the evolution of the ring current. The Dst index is derived from ground-based magnetometer measurements, and is the most widely used proxy to characterize the ring current, and thus the state of solar wind-magnetosphere interactions. The Dst index is presented as hourly averages of horizontal magnetic perturbations measured at four widely spaced, off-equatorial ground stations [*Sugiura and Kamei*, 1991]. Magnetic perturbations generated by the ring current are major contributors to the Dst index. The well-known Dessler-Parker-Sckopke relation shows that Dst is proportional to the total energy stored in the ring current [*Dessler and Parker*, 1959; *Sckopke*, 1966; *Wolf*, 1995]. Other systems that contribute to Dst include the magnetopause, cross-tail, and field-aligned currents as well as local induction effects [*Araki et al.*, 1993; *Turner et al.*, 2000; *Ohtani et al.*, 2001; *Häkkinen et al.*, 2002; *Tsyganenko and Sitov*, 2005].

[3] Many recent studies have focused on the relative contribution of the partial ring current, showing that it plays a dominant role during magnetic storms. For example, *Liemohn et al.* [2001] found that more than 80% of magnetic depressions near Dst minima are due to the partial ring current. *Le et al.* [2004] showed that whenever Dst reaches −100 nT, the total partial ring current is about three times stronger than the total symmetric current. However, due to the spatial and temporal averaging used in calculating Dst information about the local time variations of the ring current is not reflected in the Dst index. Consequently, Dst is still widely regarded as a measure of the symmetric ring current.

[4] *Iyemori* [1990] and *Iyemori and Rao* [1996] introduced similar ground-based indices, derived from measurements

[1]Space Weather Laboratory, Heliophysics Science Division, NASA Goddard Space Flight Center, Greenbelt, Maryland, USA.
[2]Space Vehicles Directorate, Air Force Research Laboratory, Hanscom AFB, Massachusetts, USA.
[3]Institute for Scientific Research, Boston College, Chestnut Hill, Massachusetts, USA.
[4]National Geophysical Data Center, NOAA, Boulder, Colorado, USA.
[5]GFZ German Research Centre for Geosciences, Potsdam, Germany.

Copyright 2011 by the American Geophysical Union.
0148-0227/11/2011JA017026

at six midlatitude stations that describe both symmetric (SYM-H) and asymmetric (ASY-H) disturbances ascribable to the ring current. The wider longitudinal coverage of contributing ground stations and 1 min reporting rates often make SYM-H more useful than Dst. The ASY-H index measures the range between observed maximum and minimum deviations from SYM-H, and is often used as an indicator of ring current asymmetry. While indicating the partial ring current's strength, ASY-H says nothing about where it peaks in local time (LT).

[5] Local time variations of magnetic field disturbances are useful for understanding the formation and evolution of the storm time ring current. In a statistical examination of how magnetic perturbations vary with local time at geosynchronous altitude, *Ohtani et al.* [2007] demonstrated strong day-night asymmetries during both main and recovery phases. The degree of asymmetry is much stronger during the main phase. They attributed the dawn-dusk asymmetry observed at low-latitude and midlatitude ground stations to the shielding effect of field-aligned currents that close the partial ring current through the ionosphere [*Wolf et al.*, 2007].

[6] Recently *Burke et al.* [2011] showed that a space-based proxy for provisional Dst can be extracted from magnetic perturbations sampled as Defense Meteorological Satellite Program (DMSP) spacecraft cross the dip equator at 840 km. While southward perturbations measured during the main phases of storms are consistently stronger in the dusk than dawn MLT sector, the coverage provided by DMSP proved too narrow to fully specify the ring current's distribution in local time. *Love and Gannon* [2010] addressed this issue using simultaneous magnetic field measurements from 25 low-latitude ground stations to map time-dependent field disturbances as functions of local time during magnetic storms. Reported local time variations of storm time magnetic disturbances display substantial variability and complexity that depend on storm phases as well as the structure of individual storms. A feature common to most storms reported by *Love and Gannon* [2010] and *Burke et al.* [2011] is a strong dawn-dusk asymmetry during main phases that decreases during recovery.

[7] Here we report on both local time and orbit-averaged variations of storm time magnetic fields observed in the low-latitude ionosphere with the triaxial fluxgate magnetometer onboard the Communications/Navigation Outage Forecast System (C/NOFS) satellite. We demonstrate that C/NOFS magnetometer measurements allow near real time information about the ring current's LT variability as well as the Dst index. The World Data Center at the University of Kyoto publishes Dst at two levels of maturity: "Real-time Quick-look" and "Final" Dst. "Quick-look" Dst is available in near real time. Currently, "Final" Dst data are available only through 2008, or about 3 years after the times of data recordings. The present analysis focuses on data acquired after April 2008, so reported comparisons are mostly with real-time, not final, Dst. However, since the C/NOFS-based proxy replicates real-time Dst to a high degree, in practical application scenarios data latency would be reduced.

[8] The remainder of this paper is divided into four parts. Section 2 describes the C/NOFS spacecraft, its scientific magnetometer payload, the POMME (Potsdam Magnetic Model of the Earth) model used to establish in-flight calibrations of the sensor and the methods used to extract magnetic perturbations from the data stream. Section 3 provides examples of C/NOFS measurements acquired during four representative magnetic storms between 2008 and 2010. We demonstrate very high correlations (≥0.96) between measured northward magnetic perturbations (δB_N) and provisional or quick-look Dst. The local time distributions of δB_N measurements are shown to be similar to those reported by *Love and Gannon* [2010]. Section 4 comments on the quality of the C/NOFS-based proxy for Dst and the feasibility for using δB_N distributions to increase understanding of ring current asymmetry. Section 5 summarizes new C/NOFS observational results and present understanding of their physical significance.

2. C/NOFS Data Reduction

[9] The C/NOFS spacecraft was launched into a nearly circular 13° inclined orbit on 17 April 2008 with a scientific payload designed to help specify and forecast plasma density irregularities in the equatorial ionosphere that degrade transionospheric radio transmissions [*de La Beaujardière et al.*, 2004, 2009]. The satellite is 3-axis stabilized and has an orbital period of ~97.5 min. Initial apogee and perigee were at altitudes of 867 and 401 km, respectively. The scientific payload includes a suite of sensors to monitor the distributions and dynamics of plasmas and electric fields in the low-latitude ionosphere [*de La Beaujardière et al.*, 2004]. This report only uses data acquired by the Vector Electric Field Instrument (VEFI) [*Pfaff et al.*, 2010] on the C/NOFS spacecraft.

[10] The VEFI suite on C/NOFS includes a sensitive 3-axis fluxgate magnetometer that is mounted on a 0.6 m boom. It measures the three orthogonal components of the Earth's magnetic field using 16 bit A/D converters with a dynamic range of ±45,000 nT. Magnetic field components are digitized at 1024 sample/s and then averaged onboard the spacecraft to 1 sample/s before transmission to ground. The primary objective of the VEFI magnetometer is to provide accurate and simultaneous measurements of local magnetic fields needed to determine induced $-\mathbf{V}_{\mathbf{satellite}} \times \mathbf{B}$ electric fields. This is critical for extracting the weak ambient electric fields that drive plasma dynamics in the low-latitude ionosphere. It is also needed to make accurate calculations of $\mathbf{E} \times \mathbf{B}$ drifts and rotating them into appropriate magnetic coordinates. The high quality of these C/NOFS measurements allows useful studies of magnetospheric current effects.

[11] The first step in analyses of raw C/NOFS magnetic field measurements is to calibrate them against terrestrial magnetic field models. For this task we have utilized and compared outputs of the most recently updated IGRF (International Geomagnetic Reference Field, available at http://www.ngdc.noaa.gov/IAGA/vmod/igrf.html) and the POMME-6 (the Potsdam Magnetic Model of the Earth, available at http://geomag.org/ models/pomme6.html) models. The IGRF is a model of the Earth's main field and its secular variation, and does not contain contributions from external fields. The POMME-6 model, on the other hand, includes both the main field and the contributions to the near-Earth

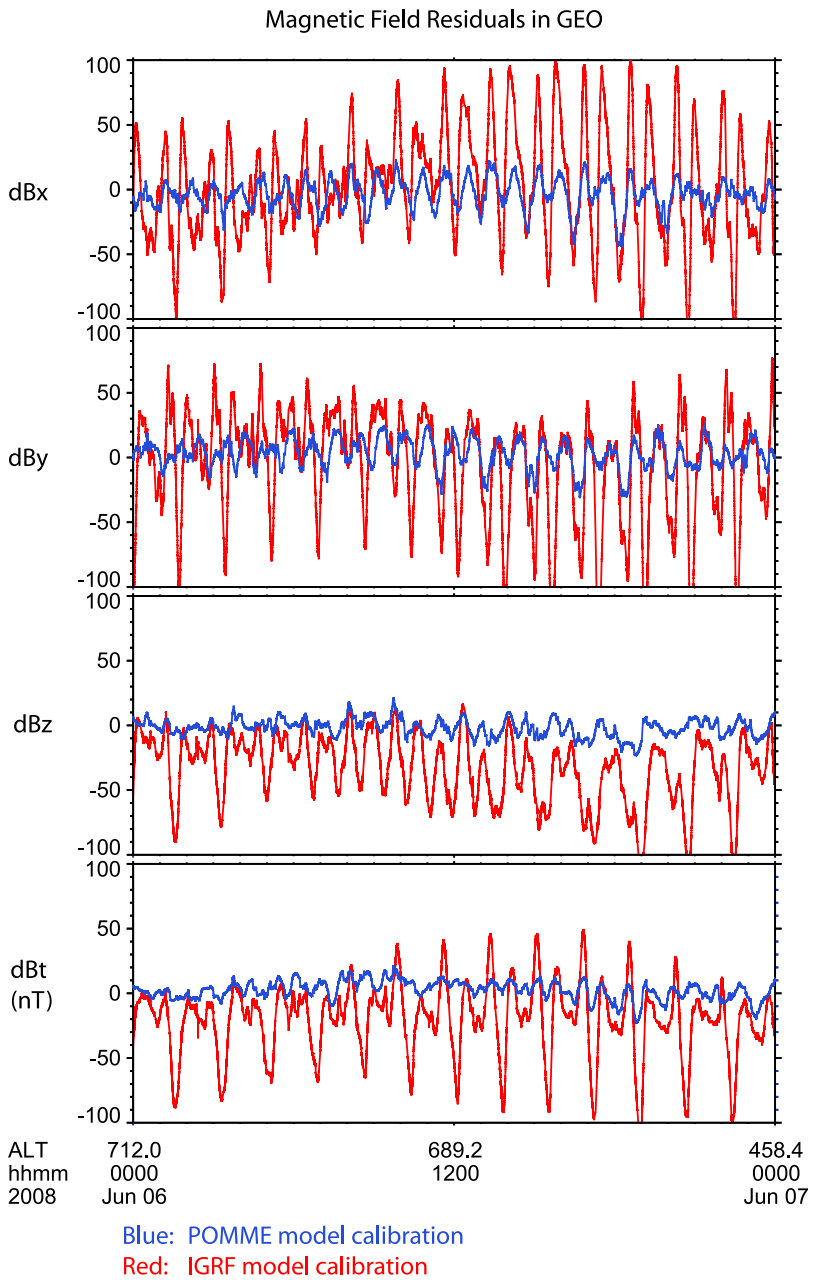

Figure 1. Comparison between the C/NOFS magnetic field data calibrated by POMME model (blue) and IGRF model (red) on 6 June 2008, a geomagnetic quiet day.

field from external current systems based on magnetic field measurements from Orsted and CHAMP [*Maus and Lühr*, 2005]. In particular, the magnetopause and ring current contribution is a constant field plus a variable part parameterized by the Dst index.

[12] The goal of the data calibration procedures is to determine a set of calibration parameters for establishing sensor gains (or conversion factors from engineering into physical units), sensor offsets (or readings at zero fields), and the nonorthogonality matrix for the sensor axes. When calibrating the C/NOFS data with the models, we apply the set of calibration parameters to the C/NOFS data to yield the corrected data (in mathematic form only at this stage), and then calculate the difference between the corrected data and the model predictions. The "in-flight calibrations" is a procedure to minimize the differences between measured and model fields on a statistical basis and yield the best fit values of the set of calibration parameters.

[13] Figure 1 shows an example of all magnetic field residuals ($\delta\mathbf{B}$) in geographic coordinates (GEO) for data acquired over the magnetically quiet day 6 June 2008. Red traces in Figure 1 represent difference between C/NOFS measurements and the IGRF model obtained after calibrating C/NOFS data against the most recent IGRF model. The plot shows that the maximum residuals are ~100 nT, a few tens of 1% of the 20,000 to 30,000 nT main field along C/NOFS trajectories. Blue traces represent differences between C/NOFS measurements and the POMME model

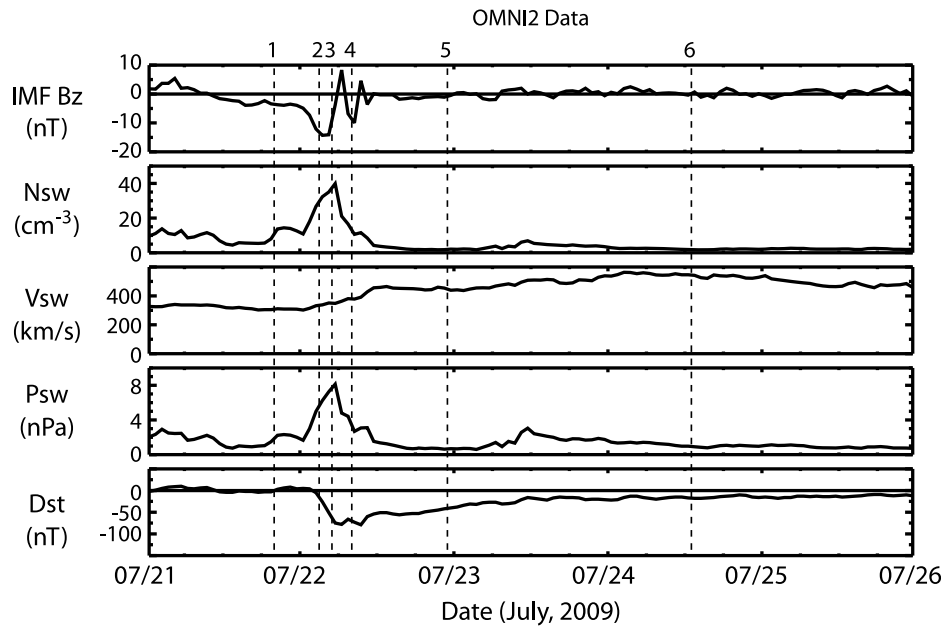

Figure 2. Overview of the 22 July 2009 storm containing 5 days of hourly averaged OMNI data from 21 to 25 July 2009. Shown from top to bottom are the interplanetary magnetic field (IMF) B_Z component; the solar wind density, N_{SW}; velocity, V_{SW}; dynamic pressure, P_{SW}; and the Kyoto provisional Dst index.

after calibrating C/NOFS data against the latest POMME model. Clearly, the quiet time residuals obtained with the POMME model calibrations are significantly lower in both the magnetic field's components and strength. These calibration results show that, on average, the POMME model accurately reproduces C/NOFS-measured magnetic field vectors to within ~20 nT, i.e., to within 0.1% in magnitude and 0.1° in direction of the main field everywhere in the low-latitude ionosphere, except in the South Atlantic Anomaly. For this reason all magnetic field data presented below were calibrated against the latest POMME model available at the time of data acquisition.

[14] After C/NOFS measurements are calibrated, we then calculate their differences from corresponding IGRF model values to study signatures of the storm time ring current. The reason for subtracting the IGRF model values from POMME-calibrated C/NOFS data is that the IGRF model represents the Earth's internal magnetic field only. Thus, resulting magnetic residuals should reflect the contributions of external currents flowing in the ionosphere and magnetosphere. During magnetic storms, the dominant contributors to these residuals are magnetic perturbations produced by the ring current. Thus, residuals enable us to study the characteristics of the ring current and its evolution.

3. Storm Time Magnetic Field Observations

[15] Data presentation in this section proceeds in two phases. We first examine LT variations of magnetic field residuals that demonstrate what can be learned about the distribution of the storm time ring current using magnetometers on satellites like C/NOFS in low-inclination orbits. C/NOFS provides coverage of all local times every orbit at a cadence that is much shorter than time scales of magnetic storms. Thus, magnetic field measurements acquired over each orbit provide information about the local time asymmetry and evolution of the ring current. In the low-latitude ionosphere, the magnetic field perturbations produced by the ring current are expected to be southward along the Earth's dipole direction, or a negative northward magnetic perturbations (δB_N). We concentrate on δB_N observed during two magnetic storms that illustrate these ring current characteristics. The second phase compares the evolution of orbit-averaged residuals with that of provisional Dst during four disturbed periods.

3.1. LT Variations of Storm Time Magnetic Field Residuals

3.1.1. Magnetic Storm of 22 July 2009

[16] The magnetic storm starting on 22 July 2009 was moderate with very simple structures. Figure 2 provides an overview of the storm, containing 5 days of hourly averaged OMNI data from 21 to 25 July 2009. From top to bottom, traces in Figure 2 show the interplanetary magnetic field (IMF) B_Z component, the solar wind density N_{SW}, velocity V_{SW}, dynamic pressure P_{SW}, and provisional Dst. The magnetic storm started shortly after the arrival of an interplanetary shock at ~01:00 UT on 22 July, as evidenced by jumps in the N_{SW} and V_{SW}. IMF B_Z turned more southward after the shock compression, changing from ~−3 to ~−15 nT. The strongly negative IMF B_Z interval lasted for ~4 h, before it underwent brief northward and southward excursions. After 12:00 UT on 22 July the magnitude of IMF B_Z became very small. Apparently the moderate magnetic storm was a consequence of the strong southward turning of IMF B_Z after the shock compression.

[17] Figure 3 shows the LT variations of the northward component of residuals (δB_N) at the six stages of the storm's development specified by vertical dashed lines in Figure 2. Plots in Figure 3 use a format similar to that introduced by

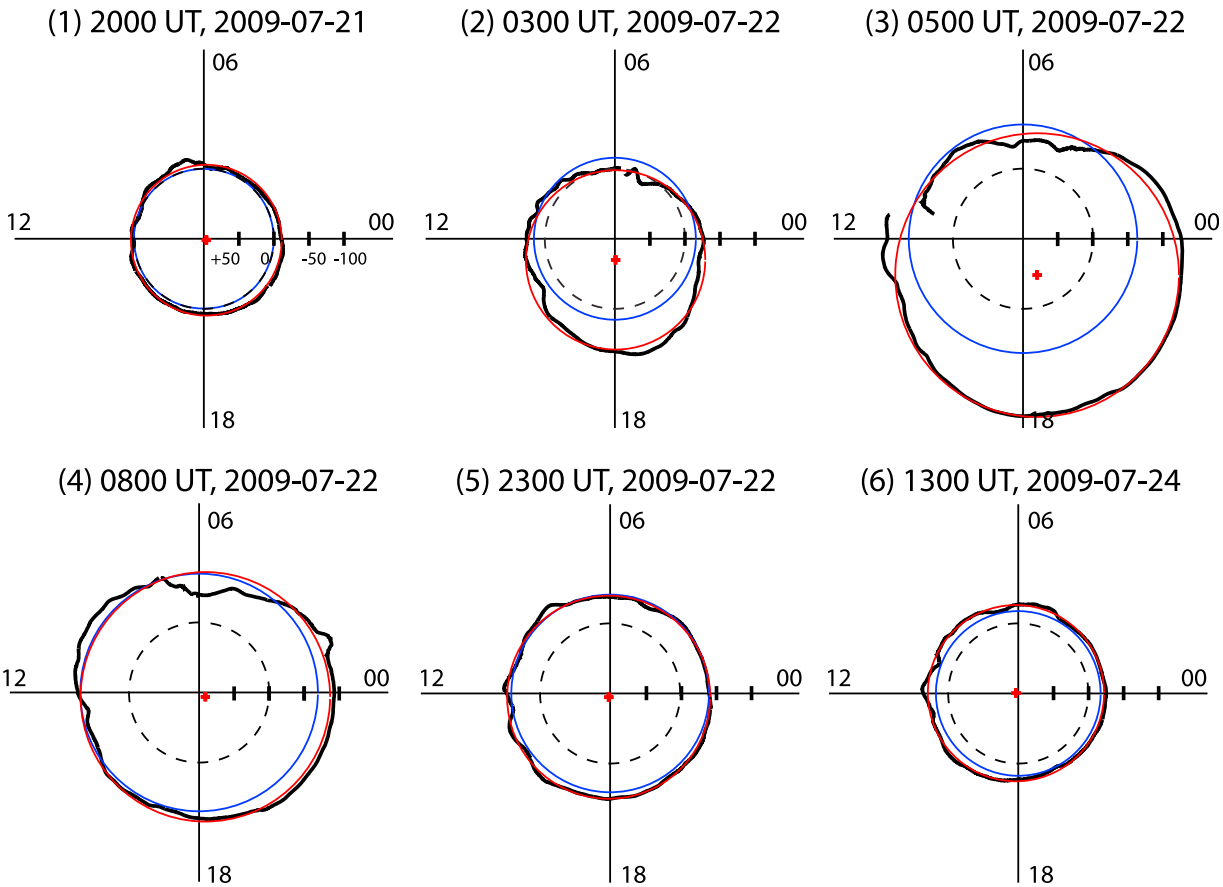

Figure 3. Local time variations of the northward component of the magnetic field residual δB_N at various stages of the storm's development. The examples correspond to the times marked by the vertical dashed lines in Figure 2.

Love and Gannon [2010]. In each panel, the time on the top corresponds to the center point of the orbit displayed. The δB_N measurements are displayed as functions of spacecraft magnetic local time (MLT) with the baseline for $\delta B_N = 0$ denoted by the dashed line circle. Positive/negative δB_N is plotted inside/outside the baseline circle. The radius of the dashed baseline circle represents a scale of 100 nT. Blue circles represent values of Dst prevailing at the universal times (UT) indicated above individual plots. Again, when the Dst index is positive/negative the blue circle lies inside/outside of the baseline circle. Thus, radial separations between the blue and baseline circles represent reported values of the provisional Dst index.

[18] Solid black traces represent δB_N plotted as a function of MLT along 97 min orbital trajectories. Similarly, the radial distance between black traces and baseline circles represent the values of δB_N with positive/negative values inside/outside the baseline circles. Since the C/NOFS orbital plane does not align with the magnetic equator, the northward residual at the spacecraft is normalized by the cosine of the magnetic latitudes where measurements were made. Thus, δB_N is the component of the magnetic field residual parallel to the geomagnetic dipole axis. Red circles in the various plots represent least squares fits to δB_N measurements. Note that off-center circles are used to fit the δB_N data, which results in two fitting parameters: the center and the radius of the fitting circle (listed in Table 1). Small red crosses mark the centers of fitted circles. The center of the fitted circle provides information about δB_N's local time asymmetry of (1) the center's MLT indicates where

Table 1. Fitting Parameters for Figure 3[a]

	Fitting Center MLT (h)	Fitting Center Displacement (nT)	Fitting Circle Radius (Baseline Removed) (nT)	Orbital-Averaged δB_N (nT)	Dst Index (nT)
Time 1, 20:00 UT, 2009-07-21	22.0	4.1	7.6	−7.6	0
Time 2, 03:00 UT, 2009-07-22	18.1	30.2	27.9	−27.0	−15
Time 3, 05:00 UT, 2009-07-22	19.4	55.6	102.4	−100.8	−63
Time 4, 08:00 UT, 2009-07-22	21.7	10.9	78.0	−77.6	−69
Time 5, 23:00 UT, 2009-07-22	16.6	5.8	44.9	−44.9	−41
Time 6, 13:00 UT, 2009-07-24	11.5	3.3	25.7	−25.6	−17

[a]Date format is year-month-day.

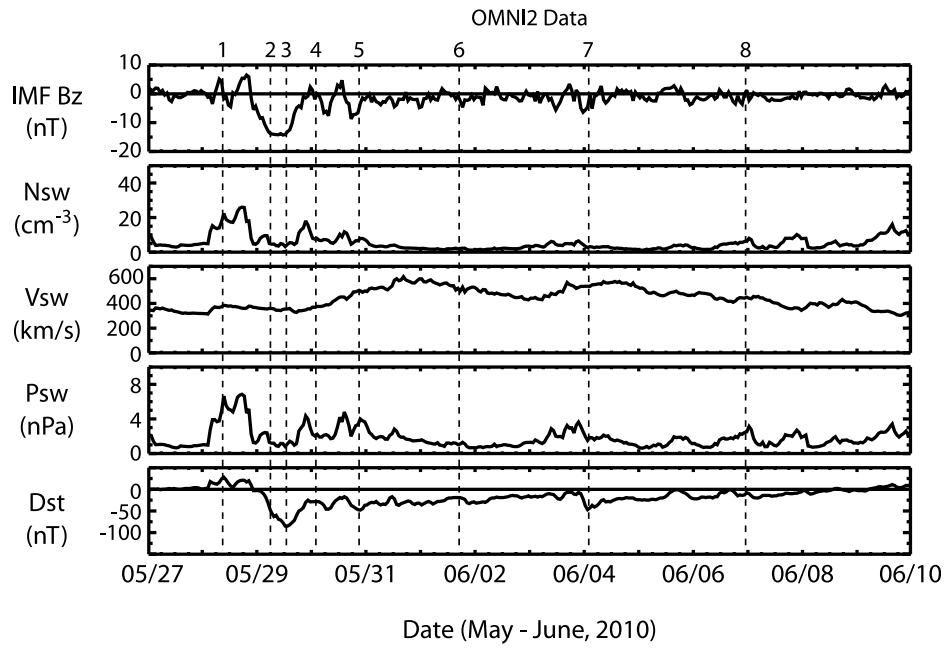

Figure 4. Overview of the 29 May 2010 storm containing 14 days of hourly averaged OMNI data from 21 to 25 July 2009. Shown from top to bottom are the interplanetary magnetic field (IMF) B_Z component; the solar wind density, N_{SW}; velocity, V_{SW}; dynamic pressure, P_{SW}; and the Kyoto provisional Dst index.

maximum δB_N occurs and (2) the magnitude of the displacement between a red circle's center from the origin is a measure of the difference between maximum and minimum δB_N, and thus the degree of the MLT asymmetry of δB_N. Radii of fitted circles (after 100 nT baseline removal) are nearly identical to the absolute value of the orbital-averaged δB_N. As an analogy to how the Dst is estimated from the ground-based dB_N, the orbital-averaged dB_N from C/NOFS data can be used as a real-time provisional Dst index. We discuss the C/NOFS provisional Dst index in more details in 3.2.

[19] Comparing time lines shown in Figure 2 with the δB_N's MLT distribution plots in Figure 3 provides a basis for perceiving the morphology of the ring current's local time evolution. The first plot in Figure 3 describes the prestorm situation when the Dst and δB_N traces were closest to the quiet time baseline. We note that even in very quiet times, the δB_N distribution indicate the ring current is slightly asymmetric. The red cross centroid was slightly shifted (4.1 nT) from the origin toward the premidnight sector where the black and red δB_N traces were ~ -10 nT. The second and third plots in Figure 3 show δB_N distributions measured during the early main phase and at maximum epoch, respectively. During the times 2 and 3 the centroid was shifted toward the dusk-evening MLT sector by 30.2 nT and 55.6 nT, respectively, a sign that the storm time ring current quickly becomes very asymmetric during the main phase. Comparing the red and blue circles we see that near the dawn meridian (where the minimum δB_N occurs) Dst was slightly more negative than δB_N. However, similar to DMSP observations [*Burke et al.*, 2011], at evening-midnight local times δB_N was significantly more negative than Dst. This asymmetry is contributed by the rapid development of a partial ring current as well as the field-aligned currents that close the partial ring current in the ionosphere. The maximum of δB_N is in the evening-midnight section during the main phase.

[20] At time 4, near the early recovery phase and a slight Dst dip to a second minimum the δB_N distribution appears to be far more symmetric than was detected during the two previous orbits. The displacement of the red cross centroid moved back to 10.9 nT. This suggests that the ring current asymmetry decreased rapidly when the first recovery began, but was not restored during the brief southward turning of IMF B_Z. Thus, the ring current recovery in this case started with a rapid decay of the partial ring current. The fifth and sixth plots indicate that during the later parts of the recovery phase the Dst and δB_N distribution traces come closer together suggesting that the ring current approached, but did not fully achieve, exact symmetry.

3.1.2. Magnetic Storm of 29 May 2010

[21] The second example comes from a more complex and extended disturbance that lasted from 28 May through 8 June 2010. This storm was the largest during the period between C/NOFS launch and the end of 2010. Data plotted in Figure 4 show that early on 28 May a sudden increase in N_{SW} and P_{SW} caused a sudden storm commencement (SSC). Because IMF B_Z was predominantly northward, a prolonged initial storm phase held the magnetosphere in a compressed state for most of the day. The main phase began late on 28 May after a sustained southward turning of IMF B_Z to -15 nT. A main phase minimum of -85 nT was reached at 13:00 UT on 29 May. Dst recovery began after a weakening of IMF B_Z south, but was followed by a sequence of minor ring current reactivations that persisted through the following 9 days. Vertical lines in Figure 4 mark eight times chosen to illustrate the temporal evolution and δB_N distribution characteristics across this disturbed period.

[22] Figure 5 shows the eight samples of δB_N versus MLT distributions using the same format as Figure 3. The

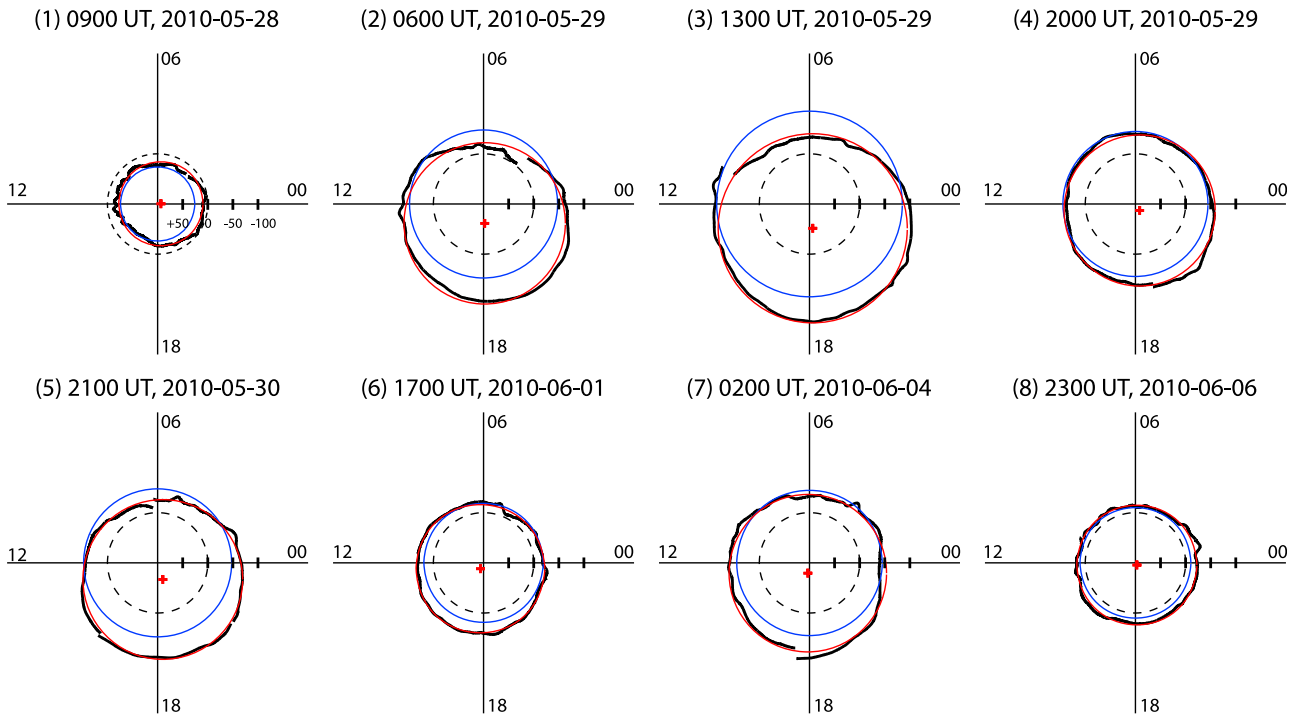

Figure 5. Local time variations of the northward component of the magnetic field residual δB_N at various stages of the storm development. Displayed plots correspond to the times of vertical dashed lines in Figure 4.

corresponding fitting parameters for δB_N are listed in Table 2. The first example at time 1 near 09:00 UT on 28 May is characteristic of the initial phase of magnetic storms when the magnetosphere is in a compressed state and prior the main phase of the storm. Except near local midnight, the red and black δB_N traces lie well inside of the baseline circle; that is, the magnetic field is enhanced due to the compression of the magnetosphere. The next two samples at times 2 and 3 show that the δB_N distribution quickly became highly asymmetric as the main phase progressed. Again, the centroid of red δB_N circles migrated toward the dusk meridian. Perspectives on the dynamics of the main phase can be obtained either by overlaying the second and third plots or by comparing the relationships between the red and black δB_N traces at the beginnings and ends of orbits. At time 2 the orbit began and ended near 04:00 MLT. Over an orbital period the black δB_N trace migrated -50 nT from near the baseline to near the red circle. Conversely, at time 3 the orbit began and ended near 10:30 MLT, and δB_N increase by +25 nT from near the blue circle to near the red circle. These changes are consistent with the ~-25 nT decrease seen in Dst trace between lines 2 and 3 in Figure 4.

[23] Subsequent episodes of recovery (4, 6, 8) and reactivations (5, 7) produced cyclical decreases and increases in $|\delta B_N|$ with levels of asymmetry, reminiscent of dynamics seen in Figure 3. At time 4 during the early recovery phase, δB_N remained to be asymmetric, but the degree of asymmetry reduced significantly comparing with the storm main phase. The fitting circle center displacement decreased to 15.4 nT at time 4 from 48.9 nT at time 3. This is an indication of rapid decay of the partial ring current as well as the associated field-aligned currents. When the ring current reactivated at time 5, δB_N distribution again became highly asymmetric, as the fitting center displacement increased to 34.8 nT. This δB_N distribution pattern repeated for recovery (times 6 and 8) and reactivation (time 7). At time 8 near the end of the recovery phase, δB_N distribution trace comes closer to the blue Dst circle but the fitting center displaced

Table 2. Fitting Parameters for Figure 5[a]

	Fitting Center LT (h)	Fitting Center Displacement (nT)	Fitting Circle Radius (Baseline Removed) (nT)	Orbital-Averaged δB_N (nT)	Dst Index (nT)
Time 1, 09:00 UT, 2010-05-28	0.2	6.5	−16.1	16.6	26
Time 2, 06:00 UT, 2010-05-29	18.2	38.7	60.8	−58.8	−47
Time 3, 13:00 UT, 2010-05-29	18.5	48.9	88.5	−85.4	−85
Time 4, 20:00 UT, 2010-05-29	20.2	15.4	50.6	−50.1	−44
Time 5, 21:00 UT, 2010-05-30	19.2	34.8	59.2	−57.7	−47
Time 6, 17:00 UT, 2010-06-01	16.1	13.3	28.2	−28.3	−19
Time 7, 02:00 UT, 2010-06-04	17.4	20.9	57.0	−56.4	−45
Time 8, 23:00 UT, 2010-06-06	20.2	5.2	19.6	−19.6	−10

[a]Date format is year-month-day.

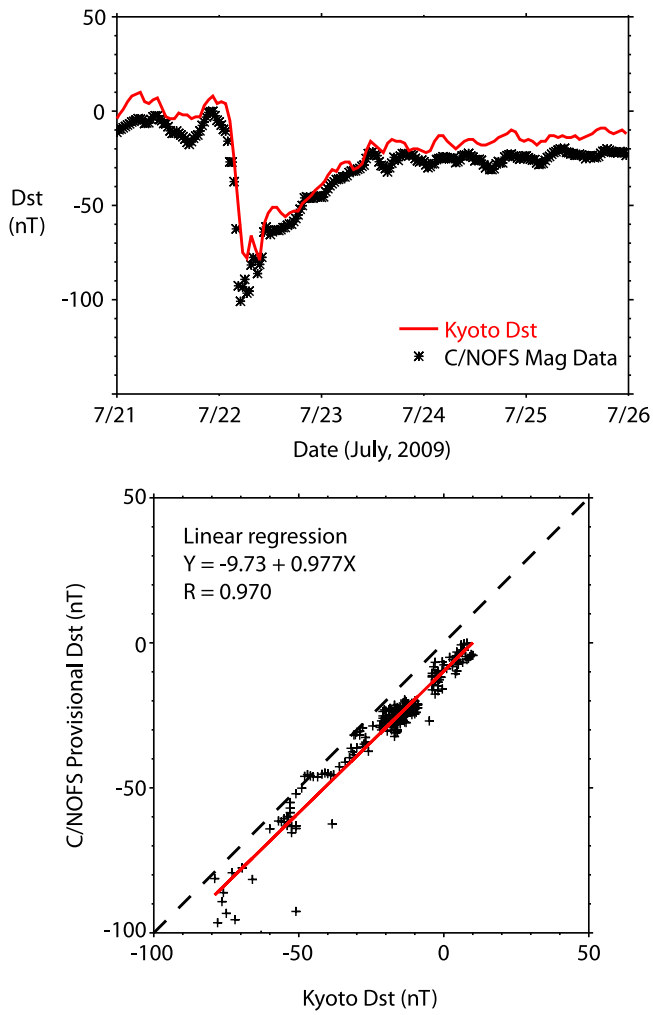

Figure 6. Comparison between the Kyoto Dst index and the δB_N proxy determined from the C/NOFS magnetic field data during the magnetic storm of 22 July 2009.

was 5.2 nT from the origin, suggesting that the ring current did not achieve full symmetry.

3.2. Provisional Dst Index From C/NOFS Data

[24] Data plotted in Figures 6–9 compare real-time Dst with orbit-averaged values of δB_N measured by the magnetometer on C/NOFS during four magnetic storms. In Figures 6–9, the orbit-averaged δB_N values have a cadence of 30 min using data from one full orbit centered at the epoch times. The hourly Dst indices are linearly interpolated to the same epoch times as the orbit-averaged δB_N. The storms of 22 July 2009 (Figure 6) and 29 May 2010 (Figure 7) are already familiar from the previously considered presentation in Figures 2–5. We also compared real-time Dst with orbit-averaged δB_N for two additional moderate storms with the main phase minima occurred on 2 May 2010 (Figure 8) and 11 October 2010 (Figure 9). Figures 6–9 display data comparisons in the same way. The top panels show real-time Dst (red lines) and orbit-averaged δB_N (black stars) plotted as functions of UT across intervals that span the prestorm though late recovery phases of the different storms. The bottom panels contain scatterplots of orbit-averaged δB_N versus Dst. Superposed on the plots are numerical and graphic (red line) results of linear regression analyses performed on the plotted data. Dashed lines with slopes of unity are provided for reference. An examination of these plots yields the following two empirical results.

[25] 1. The δB_N data points generally fell below Dst traces. This was most prevalent near storm time maximum epochs. It is also reflected in intercepts obtained through linear regression analyses that consistently ranged between −7.3 and −11.8 nT.

[26] 2. In all cases the linear regression slopes were near unity (>0.9) and the correlation coefficients were very high (≥0.96).

4. Discussion

[27] The purpose of this report has been to demonstrate the feasibility of monitoring the evolution of the ring current' distribution in local time during the different phases of magnetic storms and of extracting a proxy for provisional Dst in near real time using δB_N measurements from science-grade magnetometers on satellites in low-inclination orbits. Examples presented in Figures 3 and 5 show local time

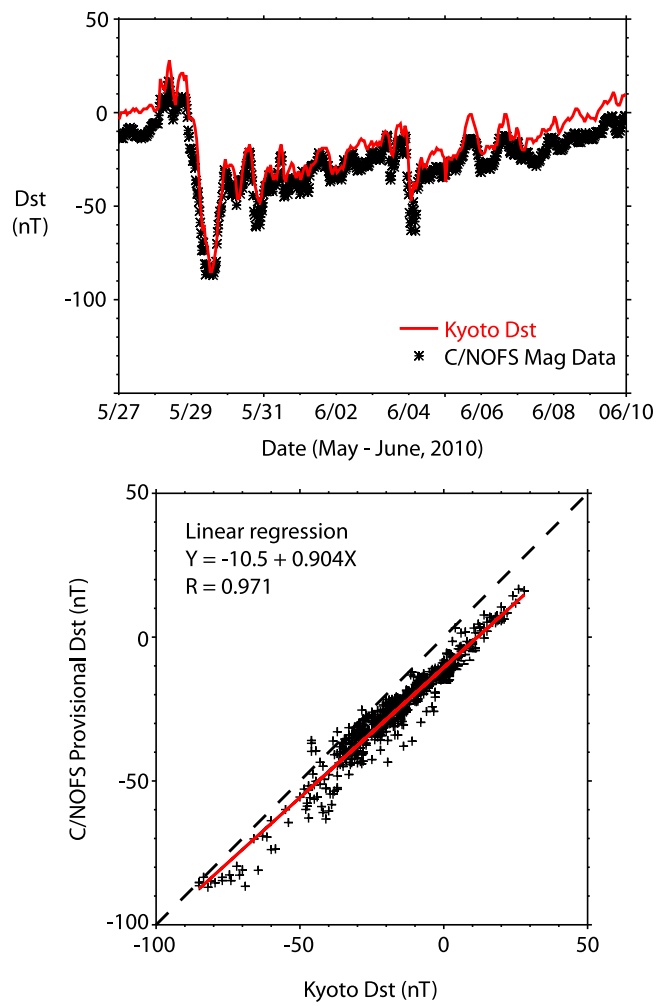

Figure 7. Comparison between the Kyoto Dst index and the δB_N proxy determined from the C/NOFS magnetic field data during the magnetic storm of 29 May 2010.

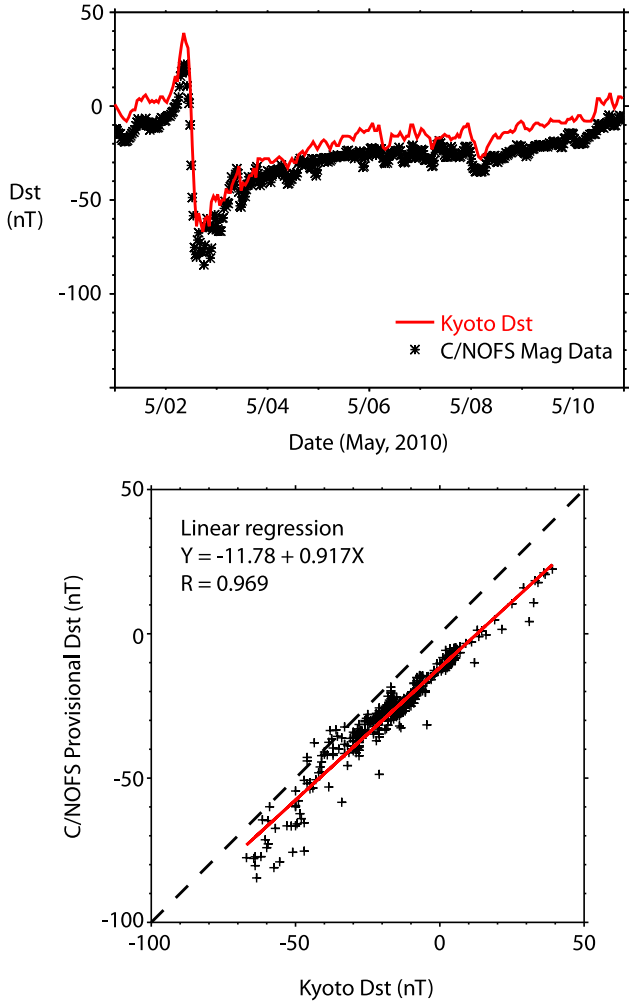

Figure 8. Comparison between the Kyoto Dst index and the δB_N proxy determined from the C/NOFS magnetic field data during the magnetic storm of 2 May 2010.

patterns in δB_N perturbations that appear consistent with analogous ground-based measurements reported by *Love and Gannon* [2010]. During the prestorm quiet period, measured δB_N distributions are very close to baselines established via up-to-date versions of magnetic field models such as POMME and/or IGRF. During the initial phase δB_N and Dst underwent positive excursions relative to the quiet time background field. As the main phases progressed the negative magnetic perturbations, indicative of the ring current, became asymmetric with the strongest δB_N perturbations found in the dusk-to-midnight local time sector. During the recovery phase the δB_N distributions quickly became more symmetric in local time and slowly decreased in magnitude toward baseline values.

[28] In this study, the peak of δB_N in the ionosphere occurs in the dusk and premidnight sectors during storms, and thus the δB_N asymmetry is predominantly between dusk and dawn. This local time characteristic is different from in situ magnetic field observations [*Le et al.*, 2004; *Ohtani et al.*, 2007] and in situ plasma observations [*Ebihara et al.*, 2002] within the ring current region at high altitudes. In particular, the in situ observations in the ring current region indicate that the partial ring current (the asymmetric current deduced from the magnetic field observations) itself centers in the midnight and premidnight sector, and the ring current asymmetry is mainly between day and night [*Le et al.*, 2004]. The geosynchronous magnetic field observations also show a day-night asymmetry during storms [*Ohtani et al.*, 2007]. The similar day-night asymmetry of the ring current is also found in simulations of plasma dynamics [e.g., *Jordanova et al.*, 2010] and empirical models [e.g., *Sitnov et al.*, 2010]. The apparent dawn-dusk asymmetry of δB_N observed on the ground and in the ionosphere is believed to be the effect of the strong field-aligned currents associated with the partial ring current and is the subject of future studies.

[29] The examples shown in Figures 6–9 demonstrate that orbit-averaged δB_N consistently replicate features found in Dst traces. In the presented examples δB_N data points usually fell below the real-time Dst traces by about 10 nT. There are two reasons for the baseline differences. First, the real-time Dst has known offsets from final Dst index. Second, such a difference is expected even with final Dst since the Dst does not consider stable magnetospheric fields such as

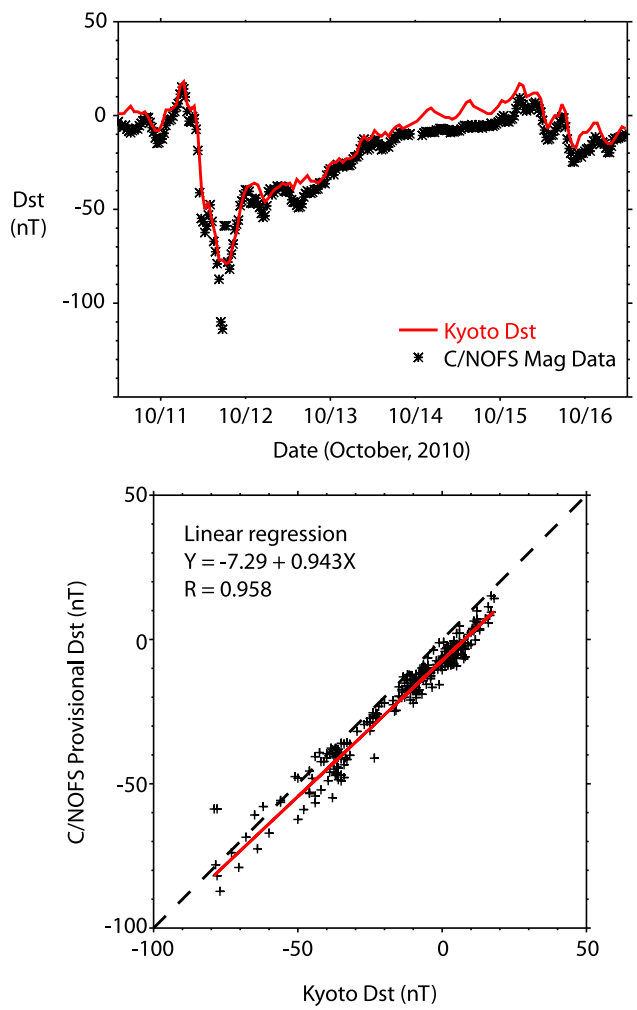

Figure 9. Comparison between the Kyoto Dst index and the δB_N proxy determined from the C/NOFS magnetic field data during the magnetic storm of 11 October 2010.

the 8 nT from the magnetotail currents and a few nT from the quiet time ring current [e.g., *Lühr and Maus*, 2010]. The facts that in all of the presented samples linear regression analyses yielded slopes slightly below unity and high-correlation coefficients attest to the fidelity attained in using δB_N measurements as proxies for provisional Dst indices. From CHAMP observations also a scaling factor around 0.9 is found between Dst and the southward component of the external field [e.g., *Maus and Lühr*, 2005].

[30] One might reasonably object that with the presented data we only demonstrated the feasibility of extracting Dst from δB_N measurements under the restricted conditions of low-to-moderate geomagnetic and having a current magnetic field model available. Indeed C/NOFS was launched under deep solar minimum conditions. Unfortunately, these conditions persisted through the first two and a half years of the spacecraft mission chosen for the present study. We note however that similar ground [*Love and Gannon*, 2010] and space [*Burke et al.*, 2011] based studies were not restricted to low-magnetic activity conditions. As mentioned above, C/NOFS-based local time distributions of δB_N measurements appear to be qualitatively similar to those reported by *Love and Gannon* [2010] during all phases of the reported storms. Also, under both moderately and strongly disturbed conditions δB_N measurements from DMSP satellites and ground station were similar to each other in the commonly sampled evening and morning local time sectors, independent of storm intensity [*Burke et al.*, 2011]. As levels of geomagnetic activity return toward solar maximum conditions we plan to continue following developments of δB_N as measured by C/NOFS. At this time, we perceive no compelling reason to anticipate failure of the C/NOFS magnetometer to accurately monitor the storm time ring current's evolution.

[31] The second concern arises from the fact that the CHAMP satellite, whose onboard magnetometer measurements were used as the basis for the POMME model, reentered the atmosphere in September 2010. For the envisaged use of data from magnetometers on low-inclination satellites to extract useful information about the local time distribution of the ring current and Dst proxies, we regard having an up-to-date model like POMME more as a convenience than a necessity. For example, *Burke et al.* [2011] used quiet time ($0 \geq \mathrm{Dst} \geq -7$ nT) measurements of δB_N acquired as DMSP satellite crossed the dip equator and IGRF 2005 to establish evolving baselines across the years 2006–2009. Correlations coefficients between provisional Dst and the DMSP-based proxies >0.95 during the studied period. In cases of satellites in low-inclination orbits, establishing a baseline is a bit more complex. Account must be taken for magnetic latitude as well as longitude variations. Standard spherical harmonic fitting procedures should make the task doable.

[32] The final question to be addressed is: "So what"? Granting that it is feasible to derive a realistic proxy for provisional Dst from δB_N measurements, what practical advantages does this capability offer? We have already alluded to the fact that the proxy provides remotely sensed information about the energy content and MLT distribution of the ring current. Knowing these two bits of information combined with regularly measured particle and magnetic field distributions at geostationary altitude will provide useful boundary conditions for improved modeling and understanding the storm time dynamics of the inner magnetosphere. A still more compelling argument can be made for obtaining real-time Dst proxy as a key for determining thermospheric drag on objects in low-Earth orbit (LEO). *Bowman et al.* [2008] showed that using the Dst index as a predictor storm time of drag effects reduced errors from about 65 to 15%. On this basis they recommended that the Air Force Space Command use Dst rather than the presently used *ap* index be used in the development of operational models used to specify and/or predict atmospheric drag exerted on space objects in low-Earth orbit (LEO) for collision avoidance [*Wright*, 2007]. The referenced studies of *Love and Gannon* [2010] and *Burke et al.* [2011] are direct responses to this challenge. Atmospheric drag and collision avoidance represent space weather issues that will be with us for the very long term. At this stage it seems prudent to explore all options for providing timely and sure access to this unexpected key to managing them.

5. Summary and Conclusions

[33] In this paper, we demonstrate that in situ magnetic field data from C/NOFS taken at low-latitude ionosphere enable us to study temporal evolution and local time variations of the ring current during magnetic storms. C/NOFS measurements consistently show that the ring current is very asymmetric during the main phase of magnetic storms. The ring current during the recovery phase quickly becomes more symmetric suggesting rapid decay of the partial ring current at the recovery. However, the data show that the ring current remains asymmetric during the quiet time and throughout the recovery phase and does not achieve pure symmetry.

[34] This paper also demonstrates that with little intervention beyond standard data reduction procedures for VEFI magnetometer measurements, we can extract a parameter δB_N whose orbit-averaged characteristics mimic those of the provisional Dst index. Correlations between Dst and the C/NOFS-based proxy consistently exceeded 0.96. Local time distributions of δB_N appear similar to those found in the different phases of magnetic storms as reported by *Love and Gannon* [2010] using simultaneous measurements 25 ground stations. This information provides remotely monitored information about the local time distribution of ring current energy in the inner magnetosphere throughout the development of large geomagnetic disturbances. The discovery that estimates of storm time atmospheric drag effects on LEO space objects are greatly improved using Dst as a model driver [*Bowman et al.*, 2008] underscores the utility of extracting δB_N as a real-time driver for orbit calculation models. Because collision avoidance is a serious and ongoing concern for all space-faring nations, the maintenance of accurate and up-to-date models of the Earth's main field is of long-term benefit to all.

[35] **Acknowledgments.** We thank Kenneth Bromund, Steve Martin, and Carmen Liebrecht for assistance in processing the C/NOFS magnetometer data. We thank the World Data Center for Geomagnetism and Space Magnetism at Kyoto University for providing Dst indices. The OMNI data are obtained from the OMNIWeb at National Space Science Data Center, NASA Goddard Space Flight Center. GSFC authors received support from the Air Force Office of Scientific Research (AFOSR) to carry out this research.

[36] Robert Lysak thanks the reviewers for their assistance in evaluating this paper.

References

Araki, T., K. Fumato, T. Iguchi, and T. Kamei (1993), Direct detection of solar wind dynamic pressure effect on ground geomagnetic field, *Geophys. Res. Lett.*, *20*, 775–778, doi:10.1029/93GL00852.

Bowman, B. R., W. K. Tobiska, F. A. Marcos, C. S. Lin, C. Y. Huang, and W. J. Burke (2008), A new empirical thermospheric density model JB2008 using new solar and geomagnetic indices, paper presented at Astrodynamics Specialist Conference, Am. Inst. of Aeronaut. and Astronaut., Honolulu, Hawaii, 18–21 Aug.

Burke, W. J., G. R. Wilson, C. S. Lin, F. J. Rich, J. O. Wise, and M. P. Hagan (2011), Estimating *Dst* indices and exospheric temperatures from equatorial magnetic fields measured by DMSP satellites, *J. Geophys. Res.*, *116*, A01205, doi:10.1029/2010JA015310.

de La Beaujardière, O., et al. (2004), C/NOFS: A mission to forecast scintillations, *J. Atmos. Sol. Terr. Phys.*, *66*, 1573–1591, doi:10.1016/j.jastp.2004.07.030.

de La Beaujardière, O., et al. (2009), C/NOFS observations of deep plasma depletions at dawn, *Geophys. Res. Lett.*, *36*, L00C06, doi:10.1029/2009GL038884.

Dessler, A., and E. Parker (1959), Hydromagnetic theory of geomagnetic storms: 1. Presented at the meeting of the AGU, May 4–7, 1959, Washington, D. C., *J. Geophys. Res.*, *64*, 2239–2252, doi:10.1029/JZ064i012p02239.

Ebihara, Y., M. Ejiri, H. Nilsson, I. Sandahl, A. Milillo, M. Grande, J. Fennell, and J. Roeder (2002), Statistical distribution of the storm-time proton ring current: Polar measurements, *Geophys. Res. Lett.*, *29*(20), 1969, doi:10.1029/2002GL015430.

Häkkinen, L. V. T., T. I. Pulkkinen, H. Nevanlinna, R. J. Pirjola, and E. I. Tanskanen (2002), Effects of induced currents on *Dst* and on magnetic variations at midlatitude stations, *J. Geophys. Res.*, *107*(A1), 1014, doi:10.1029/2001JA900130.

Iyemori, T. (1990), Storm-time magnetospheric currents inferred from mid-latitude geomagnetic field variations, *J. Geomagn. Geoelectr.*, *42*, 1249–1265, doi:10.5636/jgg.42.1249.

Iyemori, T., and D. R. K. Rao (1996), Decay of the *Dst* field of geomagnetic disturbance after substorm onset and its implication to storm-substorm relation, *Ann. Geophys.*, *14*, 608–618, doi:10.1007/s00585-996-0608-3.

Jordanova, V. K., S. Zaharia, and D. T. Welling (2010), Comparative study of ring current development using empirical, dipolar, and self-consistent magnetic field simulations, *J. Geophys. Res.*, *115*, A00J11, doi:10.1029/2010JA015671.

Le, G., C. T. Russell, and K. Takahashi (2004), Morphology of the ring current derived from magnetic field observations, *Ann. Geophys.*, *22*, 1267–1295, doi:10.5194/angeo-22-1267-2004.

Liemohn, M. W., J. U. Kozyra, M. F. Thomsen, J. L. Roeder, G. Lu, J. E. Borovsky, and T. E. Cayton (2001), Dominant role of the asymmetric ring current in producing the stormtime *Dst**, *J. Geophys. Res.*, *106*, 10,883–10,904, doi:10.1029/2000JA000326.

Love, J. J., and J. L. Gannon (2010), Movie-maps of low-latitude magnetic storm disturbance, *Space Weather*, *8*, S06001, doi:10.1029/2009SW000518.

Lühr, H., and S. Maus (2010), Solar cycle dependence of magnetospheric currents and a model of their near-Earth magnetic field, *Earth Planets Space*, *62*, 843–848, doi:10.5047/eps.2010.07.012.

Maus, S., and H. Lühr (2005), Signature of the quiet-time magnetospheric magnetic field and its electromagnetic induction in the rotating Earth, *Geophys. J. Int.*, *162*, 755–763, doi:10:1111/j.1365-246X.2005.02691.x.

Ohtani, S., M. Nosé, G. Rostoker, H. Singer, A. T. Y. Lui, and M. Nakamura (2001), Storm-substorm relationship: Contribution of the tail current to *Dst*, *J. Geophys. Res.*, *106*, 21,199–21,209, doi:10.1029/2000JA000400.

Ohtani, S., Y. Ebihara, and H. J. Singer (2007), Storm-time magnetic configurations at geosynchronous orbit: Comparison between the main and recovery phases, *J. Geophys. Res.*, *112*, A05202, doi:10.1029/2006JA011959.

Pfaff, R., et al. (2010), Observations of DC electric fields in the low-latitude ionosphere and their variations with local time, longitude, and plasma density during extreme solar minimum, *J. Geophys. Res.*, *115*, A12324, doi:10.1029/2010JA016023.

Sckopke, N. (1966), A general relation between the energy of trapped particles and the disturbance field near the Earth, *J. Geophys. Res.*, *71*, 3125–3130.

Sitnov, M. I., N. A. Tsyganenko, A. Y. Ukhorskiy, B. J. Anderson, H. Korth, A. T. Y. Lui, and P. C. Brandt (2010), Empirical modeling of a CIR-driven magnetic storm, *J. Geophys. Res.*, *115*, A07231, doi:10.1029/2009JA015169.

Sugiura, M., and T. Kamei (1991), Equatorial *Dst* index 1957–1986, *Int. Assoc. Geomagn. Aeronomy Bull.*, *40*, 1–246.

Tsyganenko, N. A., and M. I. Sitov (2005), Modeling the dynamics of the inner magnetosphere during strong geomagnetic storms, *J. Geophys. Res.*, *110*, A03208, doi:10.1029/2004JA010798.

Turner, N. E., D. N. Baker, T. I. Pulkkinen, and R. L. McPherron (2000), Evaluation of the tail current contribution to *Dst*, *J. Geophys. Res.*, *105*, 5431–5439, doi:10.1029/1999JA000248.

Wolf, R. A. (1995), Magnetospheric configuration, in *Introduction to Space Physics*, edited by M. G. Kivelson and C. T. Russell, pp. 288–329, Cambridge Univ. Press, Cambridge, U. K.

Wolf, R. A., R. W. Spiro, S. Sazykin, and F. R. Toffoletto (2007), How the Earth's inner magnetosphere works: An evolving picture, *J. Atmos. Sol. Terr. Phys.*, *69*, 288–302, doi:10.1016/j.jastp.2006.07.026.

Wright, D. (2007), Space debris, *Phys. Today*, *60*(10), 35–40, doi:10.1063/1.2800252.

W. J. Burke, Space Vehicles Directorate, Air Force Research Laboratory, Hanscom AFB, MA 01731, USA.

H. Freudenreich, G. Le, and R. F. Pfaff, Space Weather Laboratory, Heliophysics Science Division, NASA Goddard Space Flight Center, Greenbelt, MD 20771, USA. (guan.le@nasa.gov)

H. Lühr, GFZ German Research Centre for Geosciences, D-14473 Potsdam, Germany.

S. Maus, National Geophysical Data Center, NOAA, Boulder, CO 80305, USA.